High Momentum Jet Flames at Elevated Pressure, C: Statistical Distribution of Thermochemical States Obtained from Laser-Raman-Measurements

Holger Ax*, Oliver Lammel, Rainer Lückerath, Michael Severin

German Aerospace Center (DLR),
Institute of Combustion Technology,
Pfaffenwaldring 38-40, D-70569 Stuttgart, Germany

ABSTRACT

A detailed investigation on flame structures and stabilization mechanisms of confined high momentum jet flames by 1D-laser Raman measurements is presented. The flames were operated with natural gas (NG) at gas turbine relevant conditions in an optically accessible high pressure test rig. The generic burner represents a full scale single nozzle of a high temperature FLOX® gas turbine combustor including a pilot stage. 1D-laser Raman measurements were performed on both an unpiloted and a piloted flame and evaluated on a single shot basis revealing the thermochemical states from unburned inflow conditions to burned hot gas in terms of average and statistical values of the major species concentrations, the mixture fraction and the temperature. The results show a distinct difference in the flame stabilization mechanism between the unpiloted and the piloted case. The former is apparently driven by strong mixing of fresh unburned gas and recirculated hot burned gas that eventually causes autoignition. The piloted flame is stabilized by the pilot stage followed by turbulent flame propagation. The findings help to understand the underlying combustion mechanisms and to further develop gas turbine burners following the FLOX® concept. Together with the connected papers A, B and D [1–3], the results form a unique and comprehensive data set for the validation of numerical simulation models.

NOMENCLATURE

α constant for Raman evaluation
x, y, z burner coordinates
c speed of light in vacuum

*Corresponding author: holger.ax@dlr.de

d_{M} main nozzle diameter
ϵ transmission efficiency of detection optics
f focal length
f mixture fraction based on element mass fractions
$f_i(T)$ molecular Boltzmann population distribution
$G_i(T)$ Raman calibration coefficients
h Planck constant
k Boltzmann constant
L length
λ wavelength
λ air equivalence ratio
ν vibrational state
n molecular number density
n_i partial number density
ν_i wavenumber of vibrational state
Ω solid angle
P piloted flame
p pressure
P_i Raman signal intensity
$P_{c,i}$ corrected Raman signal intensity
P_L Laser intensity
q quantum efficiency of the detector
$(d\sigma_i/d\Omega)$ differential Raman cross section
T_{ad} adiabatic flame temperature
T temperature
U unpiloted flame
v nozzle exit velocity
v_x axial flow velocity
v_i vibrational state
X_i molar fraction of constituent i

Acronyms

CARS coherent anti-Stokes Raman spectroscopy
CL chemiluminescence
DLR German Aerospace Center
FLOX® flameless oxidation
GT gas turbine
HBK-S high-pressure combustion test rig of the DLR Institute of Combustion Technology
NG natural gas
PLIF planar laser induced fluorescence
PIV particle image velocimetry

1 INTRODUCTION

Gas turbines (GT) increasingly play a key role in future power generation markets. With the capability of fast startup and load changes they are well suited to balance the fluctuating power supply from wind and solar power systems and to maintain grid reliability. Heavy duty gas turbines

are also a cleaner alternative to coal based power generation for the provision of the required basic load. In order to fulfill the requirements in complex growing markets for power generation combustor concepts for modern gas turbines require a high level of both fuel and load flexibility. Fuel flexibility not only includes the capability of firing with gaseous and liquid backup fuels, but also the stable combustion of gaseous fuels of different compositions and a wide range of Wobbe indices. Operational flexibility requires the reliable operation in a wide load range while keeping the emissions below the legal limits at any time.

Gas turbine burners based on the FLOX® burner concept [4] have proven their capability to meet all requirements in various lab scale investigations and are a promising alternative to state of the art combustors [5–8]. The main design feature of combustors based on the FLOX® concept are circular arranged nozzles for a partially premixed air and fuel mixture that enters the combustion chamber with high momentum. This leads to a pronounced inner recirculation zone where hot burned gas is transported upstream and, thus, provokes ignition and stabilizes the flame by strong turbulent mixing with the unburned fresh gas. The high velocity of the fresh gas jets not only enhances turbulent mixing but also prevents flashback of the flame into the nozzles. Previous works have demonstrated the stable operation of flames even with 100 % H_2 as fuel with low NO_x emissions and without flashback in a wide operational range [8].

First feasibility studies of FLOX® burners for modern gas turbines demonstrated operation of single stage burners at high power densities and flame temperatures [9]. In the following development steps various piloted and staged burner configurations [10, 11] were tested in order to increase the operational flexibility. The evolution of FLOX® burners for GT applications has been described more comprehensively in [1].

During the current development stage, the research is focused on full size components for flexible dual-fuel injection and mixing concepts. For the present work, a new single nozzle model combustor was designed in order to optimize the access to all relevant parameters and to obtain results from both numerical simulations and high pressure tests in combination with optical and laser based combustion diagnostics. The burner design comprises several features based on the findings from previous investigations: a full-scale single nozzle of a GT burner main stage enables the test of original dual-fuel injectors. The nozzle is placed off-centered in the combustion chamber which gives space for a pronounced recirculation zone. Another feature is a pilot stage that can be operated and controlled independently from the main stage in terms of equivalence ratio and air preheat temperature.

The square combustion chamber is equipped with quartz glass windows on all four sides for good optical access that allowed for the application of optical and laser based measurement diagnostics. Several complementary measurement techniques have been applied with the aim to create an extensive data set for the validation of numerical simulations and for a detailed analysis of combustion processes like mixing, ignition and flame stabilization. For this purpose, several piloted and unpiloted flames have been investigated.

In this work, the application of one-dimensional laser Raman scattering is presented, which enables quantitative and simultaneous measurements of the major species concentration, the mixture fraction and the temperature with high spatial and temporal resolution independent from the reaction progress. The obtained results are set in relation to results of different measurement techniques that have previously been published [1, 2] and describe the flow field within the combustion chamber and the OH* chemiluminescence.

Section *Experimental Setup* of the present paper describes the investigated model FLOX® combustor and the selected operating conditions for the Raman measurements as well as the

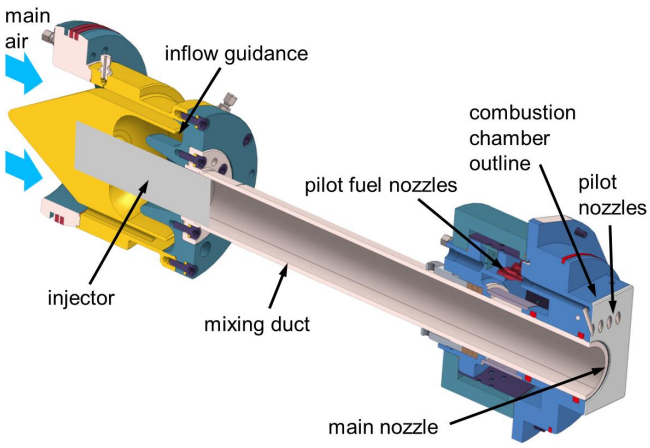

Fig. 1. Cross-section of the CJ02-burner with labeled main parts.

setup, evaluation and accuracy of the Raman measurements. In section *Results*, representative experimental results of the Raman measurements are presented and discussed in relation to the findings from other measurement techniques. The work is summarized and concluded in the last section *Summary and Conclusions*.

EXPERIMENTAL SETUP

The experiments were carried out at the high pressure combustion test rig (HBK-S) of the DLR Institute of Combustion Technology. The test rig was designed for combustion tests with different gaseous and liquid fuels up to 40 bar with a maximum combustion air mass flow of 1.2 kg/s at a maximum preheat temperature of 1000 K. The pressure casing of the test rig provides an extensive optical access in three rows on all four sides. More detailed descriptions of the test rig can be found in [1, 9, 12–14].

Model Combustor

The combustion chamber and the burner were mounted onto a test carrier that is placed inside the pressure casing for the tests. The test carrier also holds the air inflow section, the fuel supply lines and the instrumentation for monitoring the inflow conditions, material temperatures and both static and dynamic pressures. The combustion chamber has a square cross section of $95 \times 95\,\mathrm{mm}^2$ and a length of 843 mm from the burner base plate to the exhaust gas nozzle, see also [1]. The combustion chamber itself is also equipped with quartz glass windows in a dual layer configuration on all four sides for optical access to the flame. By this, only the inner combustion chamber windows are exposed to the hot temperatures of the flame and the thicker windows in the pressure casing only have to bear the elevated pressure at moderate temperatures. The optically accessible area through one combustion chamber window was $88 \times 160\ \mathrm{mm}^2$ as indicated in Figure 2. Combustion chamber windows with different dimensions were not relevant for this work.

The burner is mounted to the combustion chamber by inserting the square burner front plate into a square opening of the combustion chamber frame. A cross-section of the burner is shown in Figure 1. The single nozzle of the burner main stage consists of a stainless steel tube with a constant diameter of $d_M = 40$ mm. A multi-fuel injector for both liquid and gaseous fuels is located

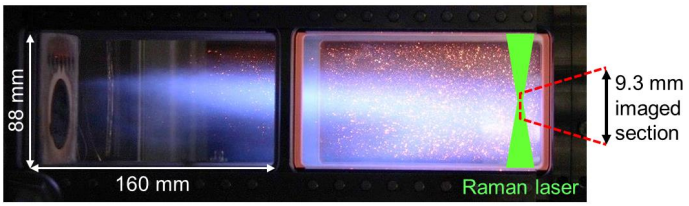

Fig. 2. Flame luminescence (photo) of the unpiloted flame. The laser beam for Raman measurements and the imaged section around the focal area is schematically indicated on the ride hand side.

400 mm upstream from the nozzle exit. In this work, only NG was used as fuel and injected in a jet in crossflow configuration (CJ02GAS1 in [1]). The long mixing duct enhances the turbulent mixing of fuel and air before the mixture exits into the combustion chamber. The mixing duct is placed with its axis out of the center of the base plate by 10 mm which gives space for a pronounced inner recirculation zone within the combustion chamber and for the nozzles of the pilot stage in the base plate.

The pilot stage consists of 7 nozzles in a row that are inclined by 60° towards the main stage. The air for the pilot stage can be preheated in a separate electrical heater and is fed from a common plenum for all pilot nozzles. The NG is fed from a separate plenum and injected by individual fuel nozzles in each of the 7 pilot nozzles. As shown in Figure 1, the separate mixing paths of pilot fuel and air after the fuel injection are long compared to the diameter of the pilot nozzles, which leads to practically perfect pre-mixing. The total air and fuel mass flows for the pilot stage can be set and controlled independently from the main stage.

The burner can be rotated by steps of 90° in the combustion chamber for an optimal optical access for combustion diagnostics. By this, measurements could be made in several orthogonal planes. The combustor and the test setup have also been described in more detail in the previous works part A and B [1, 2].

Operation Conditions

Two different flames at elevated pressure had been selected from previous works [1, 2] for detailed investigations with laser Raman scattering. The flames had already been analyzed with

Table 1. Flame operating conditions. U: Unpiloted flame; P: piloted flame.

case			U	P
Pressure	p	(bar)	8	8
Adiabatic flame temp.	T_{ad}	(K)	1900	1970
Global air-fuel equiv. ratio	λ		1.83	1.70
Main burner				
Jet velocity	v_{jet}	(m/s)	111	111
Preheat temperature	T_{air}	(K)	725	725
Pilot burner				
Jet velocity	v_{jet}	(m/s)	-	100
Preheat temperature	T_{air}	(K)	-	633

other complementary laser based measurement techniques in order to establish a comprehensive data set of these flames: the flow field had been determined by particle image velocimetry (PIV), flame structures, quantitative OH concentrations and deduced temperatures had been measured by planar laser induced fluorescence (PLIF) on the OH radical and the flame shape and position had been visualized by the detection of the chemiluminescence from the electronically excited OH* radical. Since OH* is only formed in regions of high heat release rates, it is a good marker for the position of a flame front [15]. The results of these measurements have been presented and discussed in the connected papers A and B [1,2] along with detailed descriptions of the principles of these techniques, the experimental setup and the data evaluation.

One selected flame is unpiloted with only air and fuel through the single nozzle of the burner main stage. The second flame is piloted with additional air and fuel through the pilot stage while the settings for the main stage were kept constant. The operation conditions and flame settings for both flames are summarized in Table 1. Figure 2 shows a photo of the unpiloted flame. The fresh gas jet enters the combustion chamber from the left; the burner base plate and the main nozzle can be seen on the left hand side of the picture. In the range of the first combustion chamber window, which is indicated by the white arrows, the flame luminescence can be seen mainly along the upper side of the jet towards the large recirculation zone. Further downstream, in the range of the second combustion chamber window, the flame luminescence is brighter and fully distributed over the jet region. The according average flow field of the unpiloted flame is shown in the top image of Figure 6 in the result section, the average OH*-CL signal is shown in the bottom image of Figure 7.

Raman scattering

One dimensional laser Raman scattering was applied to the two flames in order to simultaneously measure the Raman scattered light from the major species (N_2, O_2, H_2O, NG, CO_2, CO and H_2) and, thus, determine the major species concentrations, the mixture fraction and the temperature along a line of several millimeters length.

The natural gas (NG) was treated as one species in the detection and evaluation procedure. The various hydrocarbons contained in the NG all contribute to the Raman-active C-H stretch vibration that was detected at around 630 nm. The inaccuracy associated with this simplification is relatively small because the volume fraction of CH_4 in the NG was consistently higher than 0.93 and the maximum NG mole fractions measured in the investigated flames were approximately 0.07. Thus, the mole fractions of the minor constituents of the NG were below 0.004. Additionally, the temperature dependent calibration factor of NG was also determined by measurements on unburned NG for the compilation of the calibration data set.

A schematic drawing of the experimental setup is shown in Figure 3. The main components were a laser system consisting of 6 Nd:YAG lasers, a pulse stretcher, beam forming optics, the detection optics, a spectrograph and an intensified CCD camera. The frequency doubled Nd:YAG lasers (3$\times$ Spectra Physics PIV 400) provided 6 temporally separated pulses at a wavelength of $\lambda = 532$ nm, each with a duration of 7 ns at a repetition rate of 10 Hz. The beams were spatially overlapped to one beam and temporally stretched by passing through a pulse stretcher to a pulse duration of about 350 ns in order to reduce the laser intensity at the windows and to avoid optical breakdown in the focal region. The laser beam was then focused by a combination of two perpendicularly arranged cylindrical lenses ($f = 300$ mm) to generate a “blurred” focus of an average diameter of 0.5 mm. In this way, a pulse energy of around 0.8 J could be irradiated into the com-

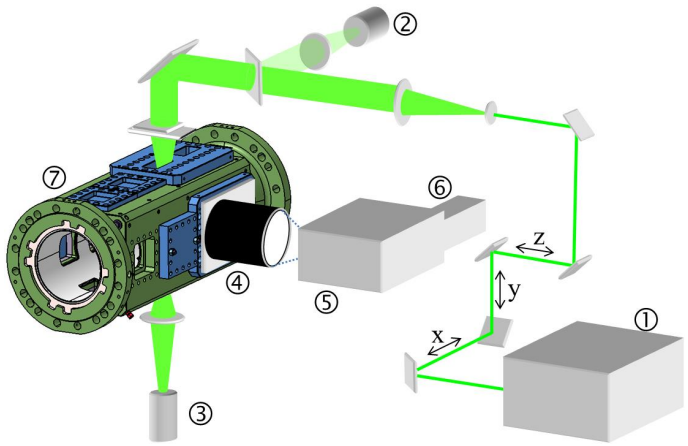

Fig. 3. Experimental setup for laser Raman measurements at the test rig HBK-S. ① laser system; ②,③ power meter; ④ achromatic lens system with IR filter; ⑤ spectrograph; ⑥ ICCD camera; ⑦ optically accessible test rig module.

bustor. The Raman scattered light was collected at 90° with an achromatic lens system with an aperture of 150 mm (Linos, custom made) and relayed onto the entrance slit of a spectrograph (Acton Research, SpectraPro 300i, 490 grooves/mm). The imaged spectral range of 163 nm covered the vibrational Stokes-Raman signal (Δv=1) of the major species. A holographic notch filter was placed in front of the entrance slit for rejection of elastically scattered light and reflections from the combustion chamber walls and windows. A slit width of 1 mm, a slit height of 14 mm and a magnification of the detection optics of 1.5 resulted in an imaged probe volume of 9.3 mm in direction of the laser beam and about 0.5 mm in diameter. After spectral separation, the Raman bands from the different major species were imaged by an intensified CCD camera (Princeton Instruments PI-MAX, Gen III intensifier, 1340×700 pixels used). The images were binned on chip to 268 superpixels in the direction of the spectral separation and 14 superpixels in spatial direction resulting in a partition of 14 measurement volumes along the laser line with 0.66 mm length each.

The laser beam was guided through the pressure housing and the combustor from top to bottom, which is schematically indicated in Figures 2 and 3. The sketch in Figure 2 also indicates the imaged section of 9.3 mm in the focal region of the laser beam. The focus was mostly kept in the middle of the combustion chamber in vertical direction. The measuring location within the combustion chamber was changed in both horizontal directions by simultaneously translating the laser beam guiding optics and detection optics via computer controlled translation stages. The three translation stages were referred to as the axes x, y and z of the Cartesian coordinate system as shown in Figure 4. The origin of the coordinate system is located on the burner base plate in the middle of the combustion chamber (see also [2]). The x-axis is in flow direction. Due to restrictions of the optical access, the closest possible measuring location to the burner was $x = 14$ mm downstream from the nozzle exit, and the evaluation of measurements up to $x < 21$ mm was complicated by nonlinear effects of shading from the pressure window flanges on the detected signal.

The results, that are presented in this report, were measured in planes with the center of the imaged section at $z = 0$ as shown in Figure 4. The 1D nature of the Raman measurement technique is indicated by the 9.3 mm “thick” planes in red, in which species concentrations and temperatures could be determined in 14 measurement volumes along the laser beam (laser di-

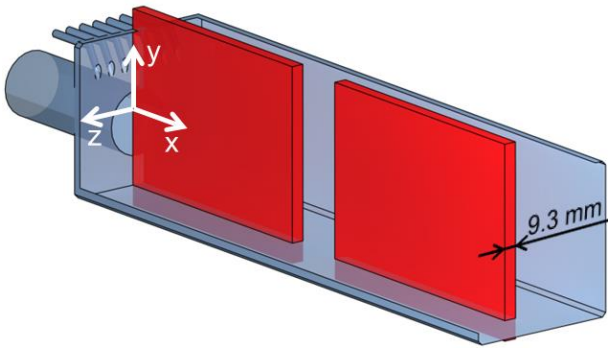

Fig. 4. Schematic drawing of the measurement locations. All measurements and results presented here were taken in planes with the center of the imaged section at $z = 0$ mm.

rection orthogonally to the indicated plane) corresponding to measurement locations in the range of $-4.65 < z < 4.65$ mm. Measurement location patterns with several hundred points in x and y direction in both the first and second window segment were compiled covering the major and relevant part of the flames and enabled the display of the results as contour plots by linear interpolation. 300 single shots were recorded at each location for a sufficient data base for a statistical single shot analysis.

Raman Data Evaluation

Due to the nature of the Raman scattering process, each species scatters the incident laser light at a different wavelength. By an appropriate selection of the grating in the spectrograph for the spectral resolution, the signal of the vibrational Raman scattering of all major species can be detected simultaneously.

A representative spectrum of the Raman scattered light after spectral resolution is shown in Figure 5 representing the signal intensities (number of counts) of the major species in dependence on the wavelength and the spatial distribution as a 3D plot. The total spectrum consists of 14 adjacent single spectra in the range of $550 < \lambda < 720$ nm. The species specific spectral ranges, that were used for the evaluation, are indicated on top and bottom of the spectrum. The 14 single spectra resulted from the on-chip pixel binning of the signal corresponding to the imaged section of 9.3 mm around the focal region of the laser beam and define the one-dimensional characteristic of the measurement technique. Thus, each of the 14 spectra marks a single measurement volume of 0.66 mm length and was individually evaluated.

The presented single shot was taken in the flame region where fresh gas mixes with hot burned gas. In the center region of the imaged section, for example, one can see strong signals of unburned NG and high peaks of N_2 because of the lower temperature and, hence, the higher density. Towards the outer measurement volumes, however, the signals of the products H_2O and CO_2 increase whereas the overall peak height decreases due to higher temperatures. In the bottom spectrum, the overall peak height increases again and a strong signal of unburned NG is detected. Thus, the 3D spectrum shows the spatial distribution of the species concentrations that result from the processes of turbulent mixing and combustion.

The number densities n_i from the different species can be derived from the rotation-vibrational

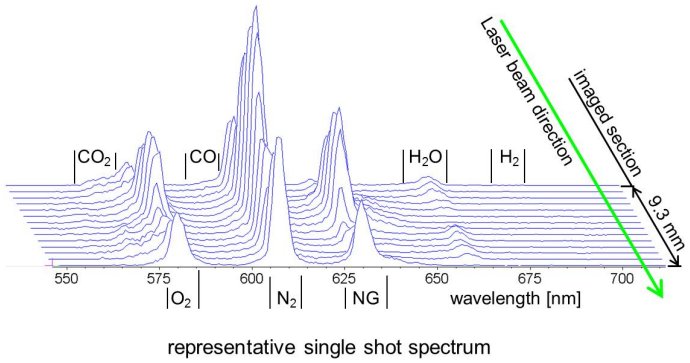

Fig. 5. Representative 1D single shot Raman spectrum consisting of 14 simultaneously imaged measurement volumes.

Raman signal intensities according to

$$n_i = \frac{P_i}{P_L \cdot (d\sigma_i/d\Omega) \cdot \Omega \cdot L \cdot \epsilon \cdot q} \tag{1}$$

with the power of the scattered Raman signal P_i, the incident laser power P_L, the differential Raman cross section $d\sigma_i/d\Omega$, the detected solid angle Ω, the length of the measurement volume L, the transmission efficiency of the detection optics ϵ and the quantum efficiency of the detector q [16]. For the quantitative evaluation of gas mixtures of different temperatures, calibration measurements were performed at known temperature, pressure and gas composition. Temperature dependent calibration and crosstalk factors (spectral overlapping of Raman signals from different species) were determined in laminar flat flames ($1150 - 2200$ K) at atmospheric conditions inside the combustion chamber. The flame temperatures had been determined beforehand with coherent anti-Stokes Raman spectroscopy (CARS) under atmospheric laboratory conditions [17,18], the equilibrium species concentrations were calculated by use of the software Gaseq [19]. The coefficients for the low temperature range ($300 - 1000$ K) were determined in cold and electrically heated gas flows for all detected species except H_2O. The temperature dependent calibration coefficients $G_i(T)$ of each species were then fitted by polynomial curves that were stored in a look-up table. The temperature dependent bandwidth factor $f_i(T)$ was taken into account by the calculation of the molecular Boltzmann population distribution according to

$$f_i(T) = \frac{1}{1 - \exp(\frac{-hc\nu_i}{kT})}, \tag{2}$$

where ν_i is the wavenumber of the vibrational state v_i, and h, k and c are the constants of Planck and Boltzmann and the speed of light in vacuum, respectively [16, 20].

The detected signal intensities P_i were integrated over species specific spectral ranges as indicated in Figure 5, corrected from crosstalk and background luminosity and weighted by the measured pressure in the combustion chamber and the laser intensity yielding the corrected signal

intensities $P_{c,i}$. The evaluation was then done by an in-house code by Eq. 1 rewritten to

$$n_i = \frac{P_{c,i}}{P_L \cdot \alpha \cdot f_i(T) \cdot G_i(T)} \tag{3}$$

with a constant α that combines all constants in Eq. 1.

The number densities of all major species are summed up to gain the total number density $n = \sum n_i$. The temperature is deduced from the total number density and the measured pressure in the combustion chamber using the ideal gas law $p = n\,kT$. The species concentrations in terms of mole fractions X_i are calculated using the ideal gas law and the partial number density, $X_i = n_i kT/p$.

For the calculation of the mixture fraction, the definition first proposed by Bilger [21] is used, which is based on the element mass fractions of C, H and O that are contained in fuel and air. This definition is implemented in the Raman evaluation software as it has advantages over other definitions in less turbulent flames where preferential molecular diffusion can occur. However, effects of preferential molecular diffusion are not expected in the flames in this work due to the high degree of turbulence, the elevated pressure and the negligible amount of hydrogen.

One of the main challenges in performing the Raman measurements was the degradation of the combustor windows which were directly exposed to the flame. At high flame temperatures quartz glass begins to soften and its surface becomes rough and increasingly opaque leading to decreasing transmittance and, in the worst case, to window damage by the laser beam due to the very high pulse energy that is needed for a sufficient signal to noise ratio. The degradation was not uniformly distributed over the window and most severe where the flame hit the quartz surface. As a result, the effective laser pulse energy at the measuring location could not always be determined accurately. Since the signals have to be weighted by the laser pulse energy, the uncertainty of the determination of the laser energy caused by degraded windows led to a significant uncertainty in the determination of the species number densities. Although the relative species composition was hardly affected by this uncertainty, the total number density and, thus, the temperature are. A similar uncertainty arose from the unknown (time and position dependent) transmission of the window on the detection side. In order to assess the impact of window staining on the signal quality and the trustworthiness of the evaluated temperatures, the laser pulse energy was measured both before and after the pressure housing of the test rig, and the ratio then compared to a reference value that was determined during the calibration measurements with clear windows. In dependence of the magnitude of the deviation from the reference value, the results were rejected or only the results of the species concentrations were used.

The precision of the Raman results can be estimated by the single shot evaluation and shot noise analysis of measurements on the stable calibration flames. The relative standard deviations in the post flame region of a lean flat CH_4/air flame at atmospheric pressure are typically around 2 % for N_2, 7 % for H_2O, 8 % for CO_2 and 5 % for the temperature and the mixture fraction. The absolute temperatures of the calibration flames were reproduced by an accuracy better than 6 %. The flame temperatures had been determined using CARS with an accuracy of 3 % [17, 18]. As the Raman signals scale linearly with pressure, the signals from the measured flames at 8 bar are a factor of 8 higher than in the calibration flames. The precision should therefore be improved by a factor of $\approx \sqrt{8}$. However, systematic uncertainties due to shifts in alignment or signal correction might impair the accuracy.

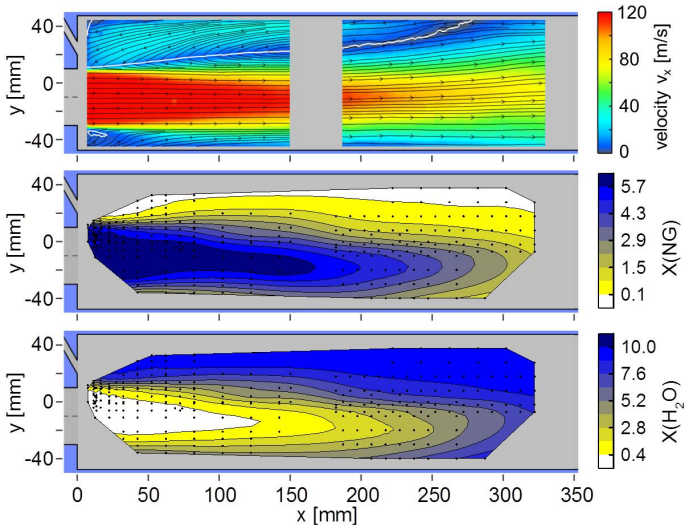

Fig. 6. Mean distribution of NG and H_2O for the unpiloted flame in comparison with the mean axial flow field. The plots share a common x-axis.

RESULTS

Unpiloted Flame, Mean Distributions

First, results of the unpiloted flame (U) will be presented. As representative results, the mean distributions of NG and H_2O are shown as contour plots in Figure 6 together with the mean axial velocity field from PIV measurements (top image). The white line in the flow field image indicates the boundary with a mean axial velocity of $v_x = 0$ between the inner recirculation zone in the top left corner and the downstream flow. The false color scales in the contour plots of the Raman results represent different levels of mole fractions; the concentrations between the measurement locations (black dots) are linearly interpolated. Only the results in one measurement volume in the middle of the imaged section along the laser beam was taken for the compilation of the contour plots that are shown here which represents a section through the combustion chamber that coincides with the plane $z = 0$ mm. The frames around the pictures schematically indicate the surrounding combustion chamber along with the position of the mixing duct and the pilot nozzles (not in use for the unpiloted flame). The concentrations across the frame between the two window segments, where also PIV could not be measured, are interpolated as for the whole contour plot.

One can clearly see the similarity of the two species concentrations regarding the shape but with opposite trends. In the case of NG, the concentration is at maximum in the region where the fresh gas mixture of air and NG enters the combustion chamber and remains on an almost constant level of around 5.6 % along the jet axis ($y = -10$ mm) downstream up to around $x = 150$ mm. The expected molar fraction of NG in the unpiloted flame based on the air and fuel mass flows and the assumption of perfect mixing is 5.5 %. Hence, the evaluated NG concentration matches the expected value very well, which supports the confidence in the results. The shear layers between the fresh gas and the hot burned gas match with the fluid dynamic shear layers (around $y = 10$ mm and $y = -30$ mm) with the highest gradients in the region between the burner nozzle downstream up to around $x = 25$ mm. The gradients in the shear layer flatten further downstream revealing an asymmetry between the two edges of the jet, whereas the mean flow field remains rather symmetric along the jet axis. On the edge towards increasing y-values, the

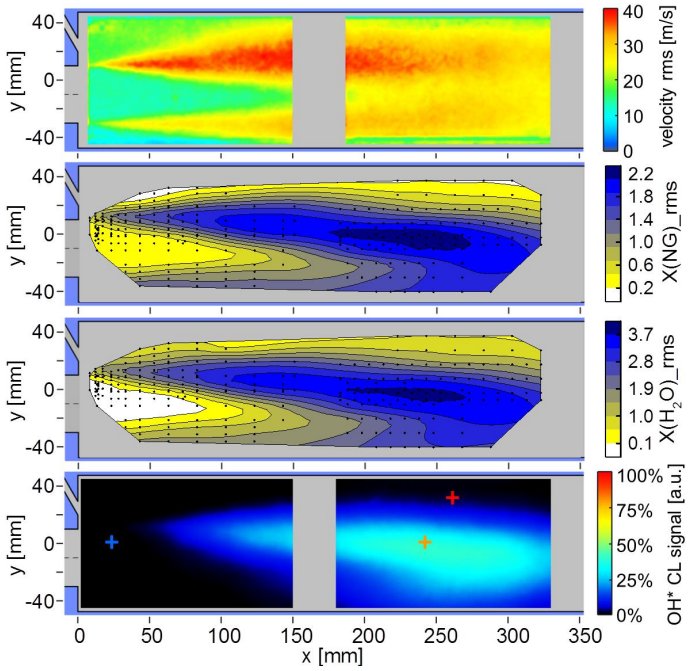

Fig. 7. Fluctuations of NG and H_2O concentrations in the unpiloted flame in comparison with the axial velocity field fluctuations and the mean OH*-CL. The crosses in the OH* image indicate the measurement locations for the scatter plots in Figure 8. The plots share a common x-axis.

gradients decrease steadily between the jet and the inner recirculation zone. Unburned NG can be found along the jet axis up to the end of the second window segment.

Water, on the other hand, cannot be found along the jet axis up to around $x = 120\,\text{mm}$. Further downstream and towards the inner recirculation zone, the water concentration increases up to the maximum of around 10 %. The gradients across the shear layers show similar trends as the NG concentration, but in opposite direction, with steep gradients between the nozzle exit and $x = 25\,\text{mm}$ and an asymmetry regarding the shear layers towards the inner and outer recirculation zones.

The concentration distributions of NG and water also indicate the mean reaction progress in the combustion chamber.

Unpiloted Flame, Statistical Evaluation

A deeper insight into the species distributions and the mechanism of flame stabilization is obtained from the statistical evaluation of the single shots. The fluctuations of the NG and water concentrations are shown in Figure 7 as contour plots together with the fluctuations of the axial velocity field and the mean OH*-CL signal. The false color scales of the fluctuations represent different levels of the root mean squares of 500 double images for the PIV measurement and 300 single shots per measurement location for the Raman measurements. The images of the fluctuations represent the distributions in the sectional plane $z = 0$, whereas the recorded OH* signal is integrated in line of sight across the whole combustion chamber.

The mixture of the fresh gas jet remains undisturbed in a thermochemical sense in a cone shaped region from the nozzle exit up to around $x = 80\,\text{mm}$. Fluctuations of NG and water con-

centrations can be found in the shear layers with increasing intensity further downstream and in particular in the shear layer between the jet and the inner recirculation zone. This is also the region where the maximum fluctuations of the velocity field can be found. Unburned NG is transported by the turbulent flow far into the inner recirculation zone leading to significant concentration fluctuations across almost the complete combustion chamber at around $x = 150$ mm. The shape of the region with high fluctuations of both NG and H_2O corresponds well with the heat release zone, marked by the OH* signal in the bottom image, which also spreads into the inner recirculation zone with its widest extent between $200 < x < 250$ mm. The strong turbulent mixing of fresh gas and burned gas in the inner recirculation zone is the key feature of flame stabilization in FLOX® concept based combustors.

The point-wise single shot evaluation enables the statistical analysis of thermochemical states of the flame with high spatial and temporal resolution. Representative results of the unpiloted flame are shown in the charts in Figure 8 at different locations, which are indicated in the OH*-CL image of Figure 7 by three crosses in different colors. The scatter plots contain the results of 300 single shots and all 14 measurement volumes ranging from $-4.65 < z < 4.65$ mm at each location. The theoretical adiabatic flame temperatures in the plotted range of the mixture fraction for NG and air are also shown as a curved line in order to facilitate the interpretation of the scatter plots. The error bars in the plots $a)$ and $c)$ indicate the mean value and the standard deviations of the evaluated mixture fractions and the temperatures.

The measurement location of the results in scatter plot $a)$ is indicated by the blue cross and lies fully within the unburned fresh gas jet. No OH* signal was detected at this location. All samples show a relatively low temperature with a mean value of 687 K and a low standard deviation of 2.3 %. The mean temperature matches well with the expected temperature considering the mixing of NG and preheated air. The evaluated mean mixture fraction of $f = 0.033$ is slightly higher than the theoretical mixture fraction of $f = 0.031$ for a perfectly premixed fresh gas with the measured air and NG mass flows. This deviation is still within the accuracy limits considering the uncertainties of the Raman measurement technique for the determination of species concentrations. However, it might also be a real deviation due to a possible leakage of combustion air into the cooling air plenum upstream of the burner resulting in a slightly richer mixture at the nozzle exit.

The indicated standard deviation of the mixture fraction is significantly higher than expected for a perfectly mixed NG/air mixture, which indicates real variations of the local mixture fraction. Compared to a reference measurement of preheated air without fuel at 8 bar, for example, the standard deviations of N_2 and O_2 in the NG/air mixture are increased by around 70 %, which indicates real variations of the local mixture.

The results shown in plot $b)$ were measured within the flame zone which is indicated by the orange cross at this position within the strong OH* signal in Figure 7. The results show a large scatter in the temperature with a somewhat bimodal distribution. One accumulation of samples lies around the low temperature of the fresh gas, another accumulation can be found close to the adiabatic flame temperature, which means that both unburned and fully reacted states can be found at this location of the flame. In between, samples with intermediate temperatures can also be found. The most probable explanation for these intermediate results is a mixture of hot burned gas and cold fresh gas in the measurement volume before ignition. Other explanations might be the crossing of a flame front separating cold unburned mixture from hot burned gas within one measurement volume, the actual process of combustion by chemical reactions during the observation time, or a conserved state after local flame extinction.

The measurements displayed in scatter plot $c)$ were taken further towards the post flame re-

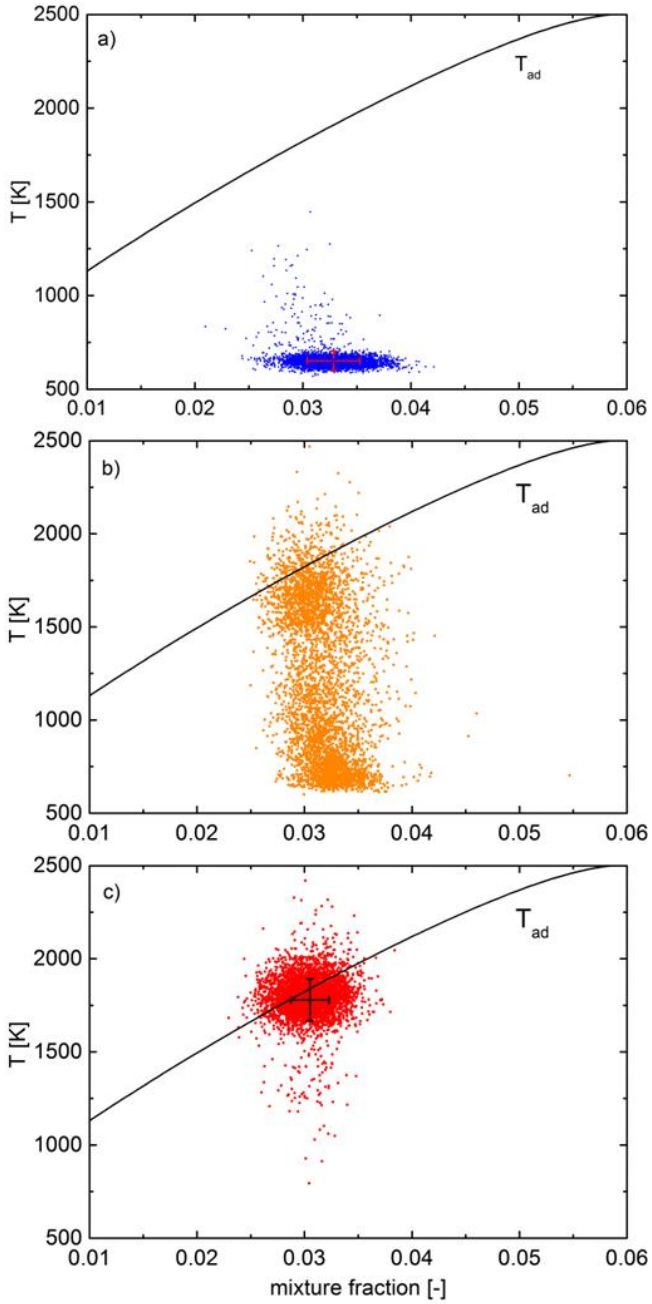

Fig. 8. Single shot evaluation of thermochemical states in different flame regions: $a)$ cold inflow conditions, $b)$ shear layer, $c)$ hot after flame region.

gion, indicated by the red cross in Figure 7. The results mostly show high temperatures around the adiabatic flame temperature, which means that the mixture is fully reacted at this location. Only a few samples with slightly colder intermediate temperatures can be found. The scatter of the results with temperatures partially above the adiabatic flame temperature is due to the inherent uncertainty of the Raman measurement technique that arises from the scattering process and the

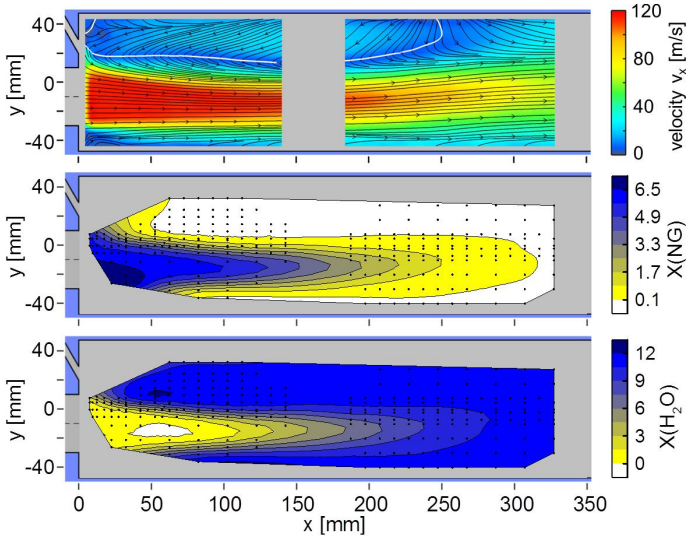

Fig. 9. Mean distribution of NG and H_2O in the piloted flame in comparison with the mean axial velocity field. The plots share a common x-axis.

photon statistics of the detection. The mean value of the mixture fraction of $f = 0.0305$ is close to the theoretical value. The discrepancy of the mean mixture fraction close to the nozzle exit and the lower mixture fraction further downstream might be due another leakage of air from the cooling air plenum into the combustion chamber across the window sealing.

The evaluated mean temperature of $T = 1779\,\mathrm{K}$ is about 120 K below the adiabatic flame temperature. Apart from the inherent uncertainty of the temperature determination by the Raman measurement technique, the hot gas temperature is indeed reduced in this configuration by cooling effects from the cooling of the combustion chamber windows and frame as well as heat loss by radiation.

Piloted Flame

The piloted flame (P) was investigated in the same plane $z = 0\,\mathrm{mm}$ and with a similar amount of measurement locations as for the unpiloted case. Figure 9 shows the mean concentrations of NG and H_2O as contour plots together with the mean flow velocity field of the piloted flame. As expected and also observed for the unpiloted flame, the concentration distributions of NG and water look similar but with opposite trends. The thermochemically undisturbed inner region of the jet is shorter than in the unpiloted flame and extends only up to around $x = 50\,\mathrm{mm}$. The mean concentrations converge steadily from the nozzle exit to around $x = 250\,\mathrm{mm}$. The concentration gradients along the shear layers are rather symmetric.

Minor differences between the concentration distributions in the two flames can be found close to the burner base plate. The plotted plane coincides with the central hole of the pilot stage where additional premixed air and NG enter the combustion chamber as it can also be seen in the flow field. The gradients of the NG concentration across the shear layer towards the inner recirculation zone are less steep and unburned NG can be found up to around $y = 30\,\mathrm{mm}$ close to the burner base plate. At the opposite side of the jet, towards the combustion chamber wall, the concentrations reach the equilibrium levels of a fully reacted mixture at the end of the first window segment in the observed region. This is partially due to the effect of the outer pilot nozzles, which

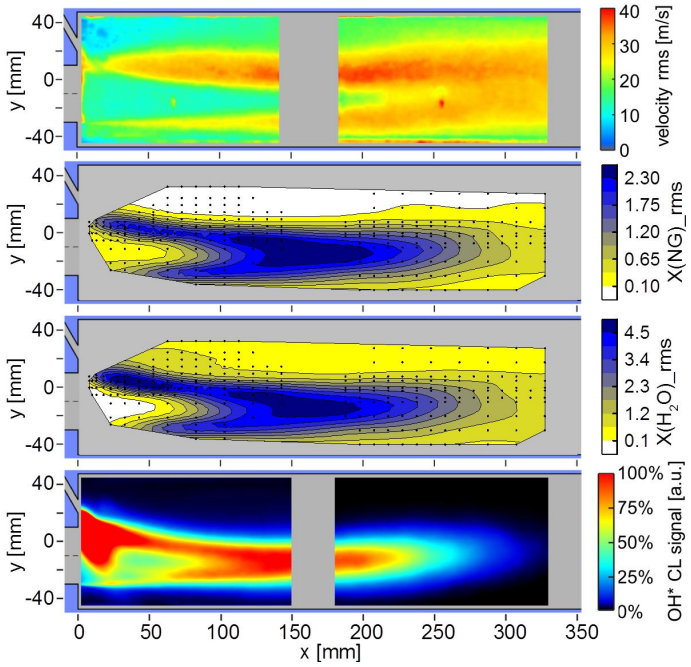

Fig. 10. Fluctuations of NG and H_2O concentrations in the piloted flame in comparison with the flow velocity fluctuations and the mean OH* CL. The plots share a common x-axis.

are positioned outside of the main stage nozzle radius. Unlike the inner pilot stage nozzles, the outer nozzles do not impinge the main stage jet, which in turn supports the ignition and stabilization of the main stage flame on both sides of the main stage jet.

The fluctuations of the NG and H_2O concentrations are shown in Figure 10 together with the mean axial velocity fluctuations (top image) and the mean OH* signal (bottom image). The impression of a somewhat constricted jet in the piloted case in comparison to the unpiloted, that was obtained from the PIV results and the OH*-CL, is also supported by the Raman results. In contrary to the unpiloted flame, the fluctuations do not spread into the recirculation zone, but are mainly restricted to the shear layers and the inner jet region. Again, the highest fluctuation intensities can be found in the same region as the highest heat release of the main flame between $100 < x < 200$ mm. The overall contour of the fluctuations is more symmetric regarding the intensities in the shear layers. Effects of the pilot stage can be found close to the burner base plate. Concentration fluctuations of both NG and H_2O on a medium level can be found on the edge of the main jet opposite from the pilot stage. Close to the pilot nozzle in the range of $20 < x < 70$ mm, the concentration fluctuations of H_2O are higher in this plane compared to the fluctuations of NG.

In comparison to the unpiloted flame, the stabilization mechanism of the piloted flame is less dominated by the mixing in the inner recirculation zone, but more by the anchoring effect of the pilot stage and subsequent flame propagation.

SUMMARY AND CONCLUSIONS

A generic burner with a single nozzle of a FLOX® combustor and a pilot stage was operated under gas turbine relevant conditions with the purpose of testing original dual-fuel injectors and mixing concepts. Optical access to the combustion chamber allowed for the investigation and char-

acterization of single unpiloted and piloted flames of a multi-nozzle burner regarding mixing, flame stabilization, flame structures and emissions. As part of extensive studies on this configuration with several complex laser based measurement techniques, one-dimensional Raman scattering has been applied in order to simultaneously determine the major species concentrations, the mixture fraction and the temperature with high spatially and temporally resolution.

Laser Raman measurements have been performed on both an unpiloted and a piloted flame at hundreds of measurement locations in several sectional planes through the flames. The evaluation on single shot basis allowed for a statistical analysis of mean values and fluctuations. Linear interpolation between the measurement locations was applied for a two-dimensional presentation of the results.

The results of the unpiloted flame show a highly asymmetric distribution of the concentration fluctuations with respect to the fresh gas jet. The fluctuations reveal a strong turbulent transport of unburned fresh gas far into the pronounced recirculation zone. The findings clearly demonstrate the underlying flame stabilization mechanism that is driven by the intense turbulent mixing of recirculated hot burned gas and fresh gas.

The effect of the inner recirculation on the flame stabilization in the case of an unpiloted flame is even more evident in comparison to the distributions of the major species concentration in a piloted flame. Though the flow field is similar in both cases, the species concentrations and their fluctuations in particular show significant differences. Natural gas, for example, is not significantly transported into the inner recirculation zone; turbulent mixing and subsequent combustion is limited to the extent of the mean flow field of the main jet.

The results add to a comprehensive data set that is valuable for the validation of models for numerical simulations and contributes to a deeper understanding of the underlying combustion processes of jet stabilized confined flames. Especially the scatter plots with the results of the instantaneous single shot measurements are of high importance for the determination of the thermochemical states within the flames and laser Raman scattering is virtually the only measurement technique for combustion processes with such a high information density.

ACKNOWLEDGEMENTS

The investigations were conducted as part of the joint research program Siemens Clean Energy Center (CEC). The work was supported by the Bundesministerium für Wirtschaft und Energie (BMWi) as per resolution of the German Federal Parliament under Grant No. 03ET7011D. The authors gratefully acknowledge Siemens AG Energy Sector for the support and permission to publish this paper.

The authors would like to thank S. Peukert and T. Schiek for the installation as well as R. Schieferstein for the test rig operation.

REFERENCES

[1] Lammel, O., Severin, M., Ax, H., Lückerath, R., Tomasello, A., Emmi, Y., Noll, B., Aigner, M., and Panek, L., 2017. “High Momentum Jet Flames at Elevated Pressure, A: Experimental and Numerical Investigation for Different Fuels”. *ASME Paper no. GT2017-64615*.

[2] Severin, M., Lammel, O., Ax, H., Lückerath, R., and Aigner, M., 2017. “High Momentum Jet Flames at Elevated Pressure, B: Detailed Investigation of Flame Stabilization with Simultaneous PIV and OH LIF”. *ASME Paper no. GT2017-64556*.

[3] Schäfer, D., Gounder, J. D., Lammel, O., Ax, H., Lückerath, R., and Aigner, M., 2019. "High Momentum Jet Flames at Elevated Pressure, D: Simultaneous Measurements of OH/PAH PLIF and Mie Scattering on Liquid Fuels". *ASME Paper no. GT2019-91177*.
[4] FLOX® is a registered trademark of WS Wärmeprozesstechnik GmbH, Renningen, Germany.
[5] Schütz, H., Lückerath, R., Noll, B., and Aigner, M., 2007. "Complex Chemistry Simulation of FLOX®: Flameless Oxidiation Combustion". *Clean Air International Journal on Energy for a Clean Environment,* **8**(3), p. 239ff.
[6] Lückerath, R., Meier, W., and Aigner, M., 2008. "FLOX® Combustion at High Pressure with Different Fuel Compositions". *Journal of Engineering for Gas Turbines and Power,* **130**(1), pp. 011505–1 – 011505–7.
[7] Schütz, H., Lückerath, R., Kretschmer, T., Noll, B., and Aigner, M., 2008. "Analysis of the Pollutant Formation in the FLOX® Combustion". *Journal of Engineering for Gas Turbines and Power,* **130**(1), pp. 011503–1 – 011503–9.
[8] Lammel, O., Rödiger, T., Stöhr, M., Ax, H., Kutne, P., Severin, M., Griebel, P., and Aigner, M., 2014. "Investigation of Flame Stabilization in a High-Pressure Multi-Jet Combustor by Laser Measurement Techniques". *ASME Paper no. GT2014-26376*.
[9] Lammel, O., Schütz, H., Schmitz, G., Lückerath, R., Stöhr, M., Noll, B., Aigner, M., Hase, M., and Krebs, W., 2010. "FLOX® Combustion at High Power Density and High Flame Temperatures". *Journal of Engineering for Gas Turbines and Power,* **132**(12), p. 121503ff.
[10] Rödiger, T., Lammel, O., Aigner, M., Beck, C., and Krebs, W., 2013. "Part-Load Operation of a Piloted FLOX® Combustion System". *Journal of Engineering for Gas Turbines and Power,* **135**(3), pp. 031503–1.
[11] Schütz, H., Lammel, O., Schmitz, G., Rödiger, T., and Aigner, M., 2012. "EZEE®: A high power density modulating FLOX® combustor". *ASME Paper no. GT2012-68997*.
[12] Fleck, J., Griebel, P., Steinberg, A., Stöhr, M., Aigner, M., and Ciani, A., 2010. "Experimental Investigation of a Generic, Fuel Flexible Reheat Combustor at Gas Turbine Relevant Operating Conditions". *ASME Paper no. GT2010-22722*.
[13] Lückerath, R., Lammel, O., Stöhr, M., Boxx, I., Stopper, U., Meier, W., Janus, B., and Wegner, B., 2011. "Experimental Investigations of Flame Stabilization of a Gas Turbine Combustor". *ASME Paper no. GT2011-45790*.
[14] Ax, H., Stopper, U., Meier, W., Aigner, M., and Güthe, F., 2010. "Experimental Analysis of the Combustion Behavior of a Gas Turbine Burner by Laser Measurement Techniques". *Journal of engineering for gas turbines and power,* **132**(5), pp. 051503–1 – 051503–9.
[15] Kojima, J., Ikeda, Y., and Nakajima, T., 2005. "Basic aspects of OH(A), CH(A), and C2(d) chemiluminescence in the reaction zone of laminar methane-air premixed flames". *Combustion and Flame,* **140**, pp. 34–45.
[16] Meier, W., Prucker, S., Cao, M.-H., and Stricker, W., 1996. "Characterization of Turbulent H2/N2/Air Jet Diffusion Flames by Single-Pulse Spontaneous Raman Scattering". *Combustion Science and Technology,* **118**, pp. 293–312.
[17] Prucker, S., Meier, W., and Stricker, W., 1994. "A Flat Flame Burner as Calibration Source for Combustion Research: Temperatures and Species Concentrations of Premixed H2/Air Flames". *Rev. Sci. Instrum.,* **65**, pp. 2908 – 2911.
[18] Weigand, P., Lückerath, R., and Meier, W. *Documentation of Flat Premixed Laminar CH4/Air Standard Flames: Temperatures and Species Concentrations*. URL: `http://www.dlr.de/vt/datenarchiv/` (last accessed Jan. 10, 2019).
[19] Morley, C. *A Chemical Equilibrium Program for Windows*. URL: `http://www.gaseq.co.uk`

(last accessed Jan. 14, 2019).
[20] Eckbreth, A. C., 1996. *Laser Diagnostics for Combustion Temperature and Species*, 2 ed. Combustion Science and Technology Book Series. Taylor & Francis, New York.
[21] Bilger, R. W., 1988. "The Structure of Turbulent Nonpremixed Flames". *Proceedings of the Combustion Institute,* **22**, pp. 475 – 488.